Available online at www.sciencedirect.com
ScienceDirect
Acta Materialia 58 (2010) 2344–2354
Acta MATERIALIA
www.elsevier.com/locate/actamat

Phase volume fractions and strain measurements in an ultrafine-grained NiTi shape-memory alloy during tensile loading

M.L. Young [a,*], M.F.-X. Wagner [a], J. Frenzel [a], W.W. Schmahl [b], G. Eggeler [a]

[a] Institut für Werkstoffe, Ruhr-Universität Bochum, Universitätsstraße 150, D–44801 Bochum, Germany
[b] Department of Earth and Environmental Sciences, Materials Research, LMU Munich, Germany

Received 26 October 2009; received in revised form 7 December 2009; accepted 8 December 2009
Available online 22 January 2010

Abstract

An ultrafine-grained pseudoelastic NiTi shape-memory alloy wire with 50.9 at.% Ni was examined using synchrotron X-ray diffraction during in situ uniaxial tensile loading (up to 1 GPa) and unloading. Both macroscopic stress–strain measurements and volume-averaged lattice strains are reported and discussed. The loading behavior is described in terms of elasto-plastic deformation of austenite, emergence of R phase, stress-induced martensitic transformation, and elasto-plastic deformation, grain reorientation and detwinning of martensite. The unloading behavior is described in terms of stress relaxation and reverse plasticity of martensite, reverse transformation of martensite to austenite due to stress relaxation, and stress relaxation of austenite. Microscopically, lattice strains in various crystallographic directions in the austenitic B2, martensitic R, and martensitic B19′ phases are examined during loading and unloading. It is shown that the phase transformation occurs in a localized manner along the gage length at the plateau stress. Phase volume fractions and lattice strains in various crystallographic reflections in the austenite and martensite phases are examined over two transition regions between austenite and martensite, which have a width on the order of the wire diameter. Anisotropic effects observed in various crystallographic reflections of the austenitic phase are also discussed. The results contribute to a better understanding of the tensile loading behavior, both macroscopically and microscopically, of NiTi shape-memory alloys.

Keywords: NiTi shape-memory alloys; Tensile testing; Stress-induced martensite; Synchrotron radiation; Localized deformation

1. Introduction

Pseudoelastic NiTi shape-memory alloys (SMAs) can be found in many medical and technological devices, due to their unique mechanical properties [1–8]. Understanding the mechanical behavior of pseudoelastic NiTi SMAs is important to accurately estimate the lifetime of these devices [9–13]. Pseudoelastic NiTi SMAs used in many applications involve processing such as wire-drawing [14–17], which results in the formation of ultrafine grains. In these ultrafine-grained materials, R phase, an intermediate martensitic phase, which involves a small ferroelastic distortion of the austenitic B2 lattice structure [18], is commonly observed [1,19–21]. Thus, examining material with both ultrafine grains and R phase is of the utmost importance.

Tensile testing of pseudoelastic NiTi reveals complex behavior involving a stress-induced phase transformation from austenite to martensite, which leads to the material's impressive ability to transform pseudoelastically upon loading and completely recover upon unloading up to almost 8% strain (an order of magnitude higher than elastic recovery in most metals). Neutron and synchrotron X-ray diffraction during in situ mechanical loading is an excellent tool for observing the phase behavior and lattice strains in both shape-memory [13,22–28] and pseudoelastic [29–41] NiTi SMAs. In the latter, it has been shown that Lüders-like transformation bands result in localized strains, leading to a stress plateau in the stress–strain curve as the

* Corresponding author. Tel.: +49 234 3225910; fax: +49 23432 14235.
E-mail address: marcus.young@rub.de (M.L. Young).

1359-6454/$36.00
doi:10.1016/j.actamat.2009.12.021

bands move across the specimen [30,42–49]. Synchrotron X-ray diffraction and imaging have been used to observe lattice strains and phases in these Lüders-like transformation bands in tensile samples from cold-rolled sheets of pseudoelastic NiTi during tensile loading [30]. Khalil Allafi et al. [29] performed in situ torsion experiments using neutron diffraction on pseudoelastic NiTi and in situ tensile experiments using synchrotron X-ray diffraction on flat specimens of pseudoelastic NiTi. In these experiments, they observed incomplete austenitic phase transformation to martensite (also observed by Schmahl et al. [30]) and significant residual strain in the untransformed austenitic phase. They did not directly observe R phase in their experiments, but suggested that R phase might be present at the interface of the martensite shear bands and austenite [30]. Hasan et al. [32] performed in situ tensile experiments using synchrotron X-ray diffraction to examine the texture evolution from austenite B2 to martensite B19′ in tensile specimens from rolled sheets of pseudoelastic NiTi. Mehta et al. [33] performed in situ tensile experiments using synchrotron X-ray diffraction on stent-like component specimens consisting of pseudoelastic NiTi. In this experiment, they observed localized austenitic phase transformation to martensite. Robertson et al. [31] also observed localized strains during martensitic phase transformation using synchrotron X-ray diffraction on compact tension specimens of pseudoelastic NiTi. The lattice strain behavior of austenite has also been examined using neutron diffraction in pseudoelastic NiTi during compressive loading [34,36], where no localized deformation was observed. Raghunathan et al. [38] examined individual texture components in B2 and B19′ phases of NiTi rolled sheet during in situ tensile loading using synchrotron X-ray diffraction. Finally, it should be mentioned here that synchrotron X-ray diffraction has been used to examine the R phase only during thermal heating and cooling, where Kulkov and Mironov [22] observed lattice parameter changes in NiTi with 50.1 at.% Ni, and Khalil Allafi et al. [50] describe the spontaneous strain evolution of R phase with temperature in the framework of the Landau theory. Although critical to many practical applications, the mechanical behavior of pseudoelastic NiTi with ultrafine grains and with R phase has only briefly been examined using synchrotron X-ray or neutron diffraction [39,40].

In the present paper, we examine the mechanical behavior of ultrafine-grained pseudoelastic NiTi SMA wire using synchrotron X-ray diffraction during in situ uniaxial tensile loading and unloading. We pay special attention to localization of the stress-induced martensitic phase transformation at the stress plateau. We determine the width of this phase transformation zone, and we examine the phase volume fractions and phase lattice strains across this zone. Furthermore, we examine volume-averaged lattice strains in the austenitic B2 and martensitic R and B19′ phases and the anisotropic effects within different crystallographic directions within austenite B2 and R phases to better understand the mechanical behavior of pseudoelastic NiTi SMAs.

2. Materials and experiments

Ultrafine-grained pseudoelastic NiTi (50.9 at.% Ni) SMA wire with a diameter of 1.2 mm was purchased from Memory Metalle (Weil am Rhein, Germany). The processing of this wire and subsequent characterization by transmission electron microscopy (TEM) have been described in detail in Sawaguchi et al. [14]. Tensile testing was performed using a miniature tensile device built by Kammrath & Weiss GmbH, which can be integrated into the beam line of a synchrotron radiation facility, as described in detail in Gollerthan et al. [51]. A wire specimen with a gage length of 40 mm was tensile tested in this custom-built device at the beam line BW5 of the Hamburg Synchrotron Laboratory (HASYLAB) at the German Electron Synchrotron (DESY). In situ X-ray diffraction measurements were collected from this wire specimen during tensile loading (up to ~1 GPa, i.e. well beyond the pseudoelastic plateau) and subsequent unloading.

As illustrated in the schematic representation of the NiTi wire in Fig. 1a and b, two types of diffraction measurements were performed on the same specimen during one loading and unloading cycle. The first type of diffraction measurements involved monitoring three different fixed positions (in the center of the wire and ±14 mm away from the center; square symbols in Fig. 1a) along the wire using synchrotron X-ray diffraction throughout loading and unloading. As illustrated in Fig. 1b, the second type of diffraction measurements was performed while holding the specimen in quasi-static conditions at a constant macroscopic strain (5.7%) on the stress plateau and collecting synchrotron X-ray diffraction patterns in a step-wise manner (0.1 mm steps) over the entire phase transformation zones on both sides of the yet untransformed austenitic region.

Diffraction measurements were performed with a 99 keV ($\lambda = 0.0125$ nm) X-ray beam in transmission geometry for 60 s. An ion chamber and a diode (Keithley, Model 428) were used to locate the center of the wire and to position the wire by measuring the initial and transmitted intensity with respect to the beam. The size of the beam cross-section was $50 \times 100\ \mu m^2$ and the sample-to-camera distance was approximately 1.0 m. Complete Debye–Scherrer diffraction rings were obtained by an image plate (MAR345) of 345 mm diameter with 100 μm pixel size and 16-bit dynamic range. Calibration diffraction patterns were collected from LaB_6 (NIST Standard Reference Material SRM-660). Typical diffraction patterns are shown in Fig. 2 for a fully austenitic state ($\sigma = 40$ MPa, Fig. 2a), an austenitic state with some R phase ($\sigma = 398$ MPa, Fig. 2b), and a fully martensitic state ($\sigma = 1060$ MPa, Fig. 2c). Although the entire Debye–Scherrer rings were collected, only one quarter is shown for clarity. All diffraction peaks were identified for the austenitic B2 and martensitic R and B19′ phases, which correspond to similar crystallographic parameters reported in Dwight (powder diffraction file # 03-065-5537) [52], Goryczka and Mora-

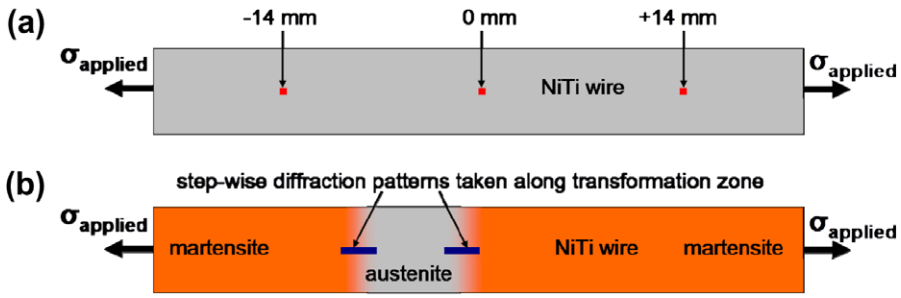

Fig. 1. Schematic of an ultrafine-grained NiTi SMA wire illustrating the two types of experiments performed on the same NiTi wire during loading and unloading. (a) First type: fixed positions (squares) along the wire were examined using synchrotron X-ray diffraction. (b) Second type: at the plateau stress (455 MPa) and at a constant macroscopic strain (5.7%), the two transformation zones between fully austenitic and fully martensitic regions were examined step-wise in 0.1 mm steps along the wire on both sides of the transformation region. The two bars indicate where diffraction patterns were collected over these transformation zones. The x-axis is parallel to the loading direction. *Note*: Schematic is not to scale.

wiec [53], and Kudoh et al. (powder diffraction file # 03-065-0145) [54], respectively. For clarity, the cell parameters from Kudoh et al. [54] are $a = 2.898(1)$, $b = 4.108(2)$, $c = 4.646(3)$, and $\beta = 97.78(4)$ and refer to a monoclinic martensite B19′ with 49.2 at.% Ni. Integration of the complete Debye–Scherrer rings recorded by the image plate was performed using the software Fit2D [55,56]. Phase volume fractions were determined for the austenitic B2 and martensitic B19′ phases by selecting isolated diffraction reflections for each respective phase, subtracting out the background, curve-fitting using a Gaussian, integrating the area under the curve, and assigning a percentage based on the value determined for this area. Lattice strains were determined by using custom MATLAB [57] programs as previously described in detail in Ref. [58] and similar to those in Refs. [59,60]. Although not shown here, lattice strain and lattice spacing vs. $\sin^2\psi$ plots were generated in order to refine the lattice parameters of each phase as described in detail in Refs. [58,61]. As illustrated in Fig. 2a–c, it should be noted that texture was observed in all three phases present (austenite B2, R phase, and martensite B19′). The texture observed in both the austenitic B2 and martensitic B19′ phases is almost identical to that observed by Hasan et al. [32]. The texture here appeared in the same location in each diffraction pattern for each specific phase during loading. Only the lattice strain and the magnitude of the intensity changed except in the case of martensite, where peak splitting (associated with twinning of the stress-induced martensite) was also observed. Since the diffraction rings were sometimes incomplete, the values reported for the lattice strains in the loading direction (ε_{11}) and transverse to the loading direction (ε_{22}) were extrapolated when necessary.

3. Results

3.1. Macroscopic stress–strain behavior

As illustrated in Fig. 3, the macroscopic stress–strain curve initially exhibits linear-elastic behavior with an apparent austenitic elastic modulus of 56 GPa (calculated from the stress–strain data ranging from 0 to 150 MPa), which is within the range of values reported in the literature ($E_{\text{austenite}} = 40$–$90$ GPa [62–64]). At a load above 150 MPa, a bend in the stress–strain curve is observed. This deviation from the linear-elastic behavior is usually attributed to a phase transformation from austenite to R phase [1,19,20]. A stress plateau (455 MPa) is reached at 1.1% strain and continues up to a strain of 5.9%. This stress plateau is associated with the stress-induced transformation from austenite (or the previously formed R phase) to martensite, which proceeds in a localized manner, where fully martensitic regions are first nucleated near the grips in our case. These martensitic bands propagate through the gage length at a constant stress [30,42–49]. After 5.9% strain is reached, the wire has become fully martensitic and the applied stress starts to increase again with increasing strain, which is associated with a macroscopically homogeneous deformation of the tensile specimen. It is difficult to determine the elastic modulus of martensite due to the fact that the martensite has already accumulated some small amount of strain before the phase transformation is complete; however, it is still possible to find a range of 25 GPa (determined from a linear fit of the data between a load of 430 MPa up to 1060 MPa) to 28 GPa (determined from a linear fit of the data between a load of 430 MPa up to 530 MPa) for the apparent slope, which is within the range of macroscopic moduli values reported in the literature ($E_{\text{martensite}} = 20$–$70$ GPa [27,62,63,65,66]). However, it should be noted that this apparent elastic modulus results from various deformation mechanisms which act simultaneously, such as elasto-plastic deformation, variant reorientation and detwinning of martensite [27,62,63,65,66]. Understanding the complex interactions between these deformation mechanisms and the stress-induced martensitic transformation is a key objective of current research activities [63,67,68].

At a maximum stress of 1060 MPa and 8.4% strain, the load is removed. During unloading, the fully martensitic tensile specimen exhibits linear-elastic behavior down to a stress of 500 MPa and 7.1% strain with an apparent martensitic elastic modulus of 43 GPa. The marked difference

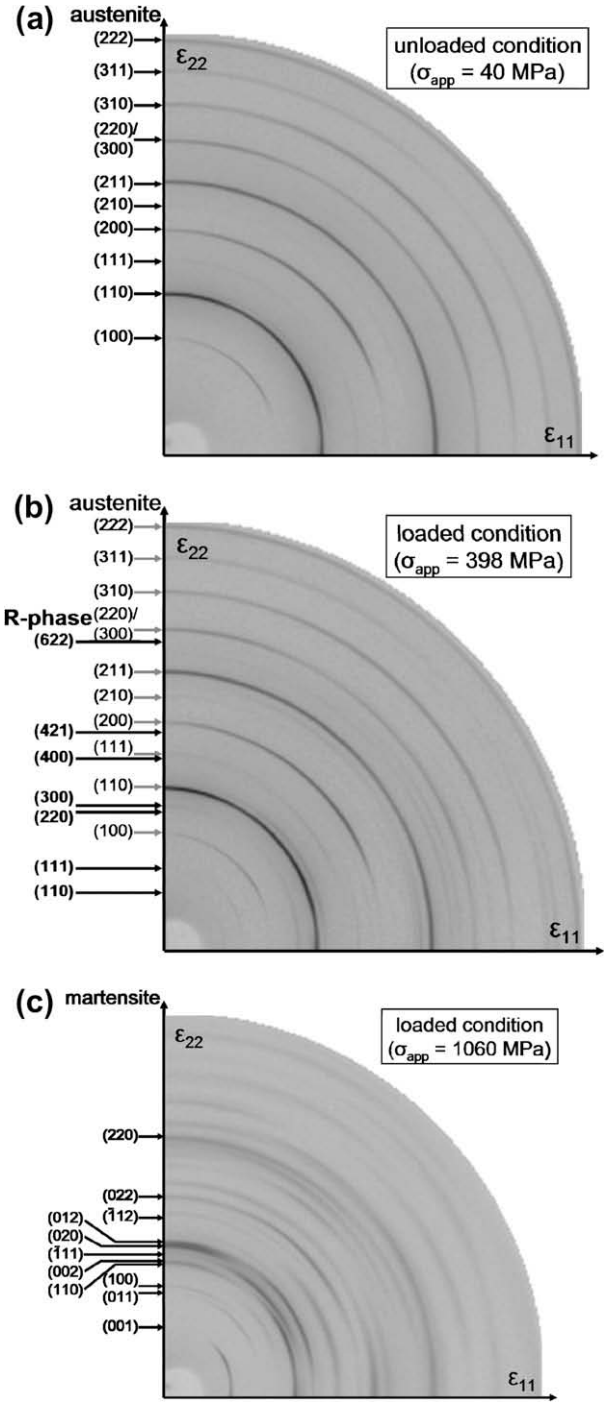

Fig. 2. Representative X-ray diffraction pattern (quarter of image plate) of (a) pure austenite B2 ($\sigma_{app} = 40$ MPa), (b) austenite with some R phase ($\sigma_{app} = 398$ MPa), and (c) pure martensite B19′ ($\sigma_{app} = 1060$ MPa) in an ultrafine-grained NiTi SMA wire. Lattice strains in the loading direction and transverse to the loading direction, represented by ε_{11} and ε_{22}, respectively, are calculated from the change in position of a respective (*hkl*) reflection during loading. All diffraction rings were identified. For clarity, only some of the rings are indicated here. Darker pixels indicate higher diffracted intensity.

between the macroscopic moduli of martensite during loading and unloading clearly indicates the importance of additional deformation processes in this regime of the stress–strain curve. Below 7.1% strain (500 MPa), nonlinear-elastic behavior is observed, which is also likely associated with inelastic deformation processes such as twin boundary movement, and possibly reverse plasticity (i.e. Bauschinger effect [69]) and dislocation movement. At 5.1% strain, an increase in stress from 50 MPa up to 100 MPa indicates nucleation of an austenitic region, which marks the beginning of the localized reverse transformation of stress-induced martensite to austenite as indicated by the stress plateau of 100 MPa from 5.1% to 0.7% strain. At 0.7% strain, the specimen is fully austenitic. Below 0.7% strain, linear-elastic behavior with an apparent austenitic elastic modulus of 45 GPa (calculated from the stress–strain data ranging from 60 to 17 MPa) is observed. After unloading is complete, approximately 0.5% irreversible strain remains. The small amount of unrecoverable strain is remarkable given the maximum amount of applied stress (1060 MPa) and strain (8.4%).

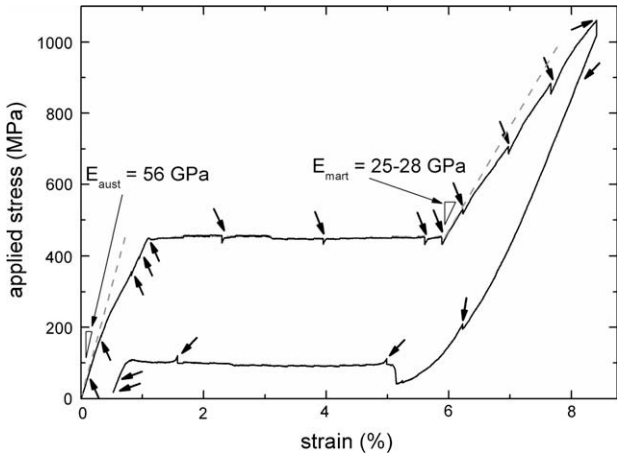

Fig. 3. Macroscopic stress–strain curve for the pseudoelastic NiTi SMA wire during tensile loading and unloading. Dashed lines are extrapolations of the linear-elastic regions. Gray arrows indicate positions along the stress–strain curve where in situ synchrotron X-ray diffraction measurements were performed.

3.2. Microscopic strain behavior

3.2.1. Elastic lattice strains in austenite and R phase

Fig. 4a shows the applied stress plotted against the lattice strain for the austenitic B2 (1 0 0), (1 1 0), (2 0 0), and (2 1 1) reflections for a fixed position ($x = 0$ mm) during loading. The slopes of the macroscopic stress plotted against the lattice spacings of the respective reflections were calculated from the first two data points only (at 40 and 177 MPa). These slopes indicate the Young's modulus for each lattice plane. For example, the slopes of the lattice plane for the (1 0 0) reflection in the longitudinal and transverse directions are $E_{11} = 53$ GPa and $E_{22} = -98$ GPa, respectively; by then using the relationship for Poisson's ratio ($\nu \approx -E_{11}/E_{22}$), a value of 0.54 for the austenite (1 0 0) reflection is found. Thus, the average Poisson's ratio from all four austenite reflections yields a relatively high value of 0.52; however, it is worth noting that the X-ray

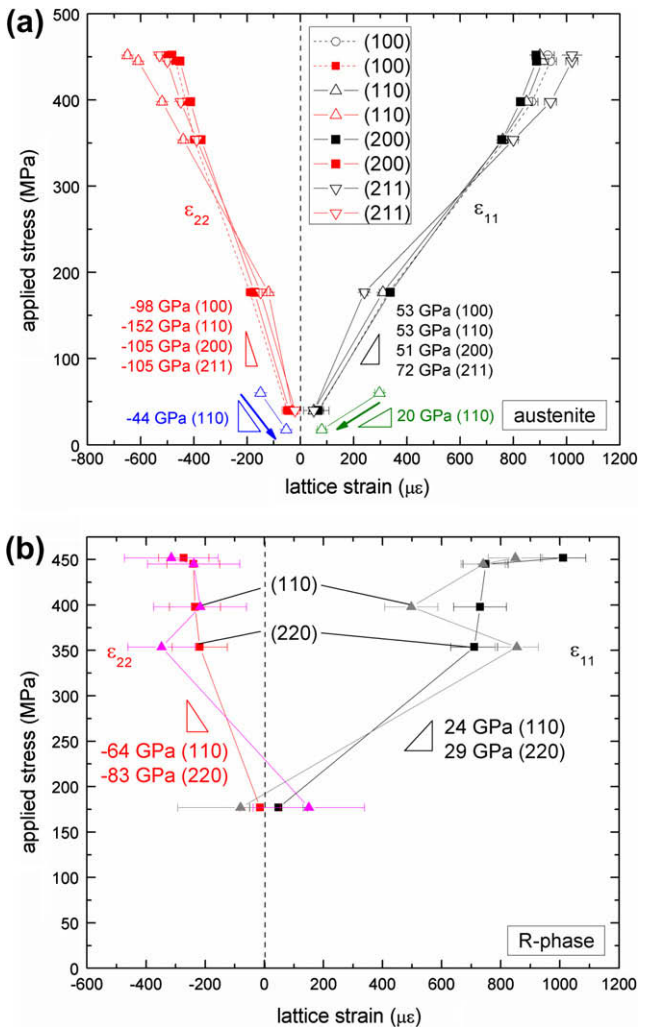

Fig. 4. Applied stress vs. lattice strain (ε_{11} parallel and ε_{22} perpendicular to the applied stress) at low load for the (a) austenitic B2 (1 0 0), (1 1 0), (2 0 0), and (2 1 1) reflections during loading (red and black colored data) and the austenitic B2 (1 1 0) reflection during unloading (green and blue colored data), and (b) R phase (1 1 0) and (2 2 0) reflections during loading. The values of the slopes represent best fit of the experimental data for the first two data points for the austenitic phase during loading, for the last two data points for the austenitic phase during unloading, and for all of the data points for the R phase, respectively.

diffraction measurements record the elastic deformation only. Although it is difficult to accurately assess the values of the slopes, since they are very sensitive and are determined from only two points, it is encouraging that the average elastic microscopic modulus (57 GPa) is approximately the same as the macroscopic austenitic modulus (56 GPa). As the applied stress is increased above 177 MPa, deviations from linearity are observed in the austenitic B2 phase, which are associated possibly with stress relaxation due to the phase transformation to R phase and its ferroelastic (inelastic) behavior. Although less likely due to the much higher yielding stress of austenite, the onset of plastic deformation of the austenitic phase cannot be ruled out.

Anisotropy can be observed between the experimental slope values of the different austenitic B2 lattice planes throughout loading, as indicated by the different strains observed for different (*hkl*) lattice planes. While the lattice spacings change, the overall texture orientation in the austenite phase does not change during loading. For the (1 0 0) and (2 0 0) lattice planes, nearly equivalent experimental slope values of 53 and 51 GPa in the loading direction, and −98 and −105 in the transverse to loading direction, respectively, are obtained as expected since these two reflections represent the same crystallographic reflection in a cubic crystal structure such as austenite. The (2 1 1) reflection exhibits a much higher Young's modulus (72 GPa) and a much larger decrease in the slope above 177 MPa as compared to those of the other lattice planes. While in the transverse direction, the (1 1 0) lattice plane shows a much larger slope (−152 GPa) and a much larger decrease in the slope above 177 MPa than those of other lattice planes.

In addition to lattice strain measurements in the austenitic B2 phase, Fig. 4b shows the applied stress plotted against the lattice strain for the martensitic R phase (1 1 0) and (2 2 0) reflections for a fixed position ($x = 0$ mm) during loading. R phase can be observed in the stress range of 177 MPa up to 455 MPa. Like the overall texture orientation in the austenitic B2 phase, the texture orientation of the martensitic R phase does not change during loading, but the strain does increase (approximately 1000 and −300 με in the loading direction and in the direction transverse to loading, respectively). The slopes of the lattice spacings of the (1 1 0) and (2 2 0) reflections were calculated from the data points from 177 MPa up to 455 MPa. They are 24 GPa and −64 GPa for the (1 1 0) reflection and 29 GPa and −83 GPa for the (2 2 0) reflection in the longitudinal and transverse directions, respectively. These values correspond to a Poisson's ratio of 0.37 and 0.28 for the (1 1 0) and (2 2 0) reflections, respectively, which yields an average Poisson's ratio of 0.32.

3.2.2. Elastic lattice strains in stress-induced martensite

Although some residual austenite (less than 4 vol.%) was detected, the NiTi wire is fully martensitic, for all practical purposes, at stresses above the plateau stress (455 MPa) and strains above 7.2% strain (Fig. 3). Fig. 7 shows the applied stress vs. lattice strain at a fixed position ($x = 0$ mm) for the martensitic B19′ (0 0 1) reflection upon loading and unloading. The elastic slopes for the martensitic B19′ (0 0 1) are 69 GPa and −176 GPa upon loading, which yields a Poisson's ratio of 0.26. After a load of 531 MPa, a deviation from linearity is observed as a result of a combination of plastic deformation, detwinning, and reorientation. At the maximum load (1060 MPa), this deviation from linearity results in a lattice strain of 230 με in the loading direction (ε_{11}) and −20 με in the transverse direction (ε_{22}), which are calculated by subtracting the linear-elastic line (dashed lines in Fig. 7) from the experimental data.

3.2.3. Elastic lattice strains during unloading

As illustrated in Fig. 7 (open data points), the martensitic B19′ (001) reflection behaves linearly elastic upon unloading down to a stress of 200 MPa, which is similar to that observed in the macroscopic stress–strain curve in Fig. 3; however, the deviation from linearity in the macroscopic data occurs at a much higher stress of 500 MPa. Below 200 MPa, the unloading data exhibits a smaller decrease in strain, which is not observed in the macroscopic stress–strain curve, where a larger decrease in strain is observed. This suggests that a number of possible mechanisms occur during unloading including stress relaxation, reverse plasticity of martensite, and reverse martensite to R phase transformation. Further experiments are needed to determine which deformation mechanisms are occurring.

As illustrated in Fig. 4, the austenite (1 1 0) reflection exhibits much softer elastic moduli (20 GPa and −44 GPa in the loading direction and in the transverse direction to loading) during unloading. These elastic moduli were calculated from the last two data points (60 and 20 MPa) only.

3.3. Localized deformation and characterization of phase transformation zones

At 455 MPa (the stress plateau), the macroscopic stress becomes constant while the macroscopic strain continues to increase from 1.1% to 5.9% strain (Fig. 3). During this macroscopic strain increase, two martensitic transformation bands are observed to move along the gage length as shown in Fig. 1b. Similar to the Lüders band propagation observed in some steels, the phase transformation bands can propagate from one end or from both ends of the wire (as is the case here), depending upon the loading speed (at higher speeds the bands tend to propagate from both ends). Micro-strain measurements at a fixed position show the lattice strain in the austenitic phase increasing until the martensitic phase transformation band propagates past this specific position.

As illustrated in Fig. 1b, additional diffraction measurements in small step sizes along the wire were collected at a constant macroscopic strain (5.7%) to observe the phase transformation regions between austenitic and martensitic regions in greater detail. Fig. 5a and b shows diffracted intensity at a constant strain (5.7%) plotted against lattice spacing for various austenitic and martensitic (*hkl*) reflections. As illustrated in Fig. 5a, it is difficult to analyze most diffraction peaks from NiTi when both phases are present due to overlapping peaks. However, a few diffraction peaks, such as the martensitic B19′ (0 0 1) in Fig. 5b, are isolated from all other diffraction peaks. By integrating the area under a single peak at various positions along the wire, it is possible to determine the phase volume fraction (e.g. the martensitic B19′ (0 0 1) reflection at $x = -7.25$ to -8.15 mm where the phase volume fraction decreases from 99% to 4%, respectively, Fig. 5b). Plotting the resulting phase volume fraction as a function of position along the wire (Fig. 5c), it is possible to determine the macroscopic width of the phase transition zone.

Fig. 6a and b shows the lattice strain for the martensitic B19′ (0 0 1) reflection as a function of position along the NiTi wire at a constant macroscopic stress (457 MPa) and strain (5.7%). Positions far away from the transformation region exhibit tensile strains in the loading direction (Fig. 6a) and compressive strains in the transverse direction (Fig. 6b) for the martensitic B19′ phase (154 and –97 με for $x = -14$ mm, 61 and -58 με for $x = 14$ mm, and 117 and -85 με for $x = 0$ mm in the loading and transverse directions, respectively). As illustrated in Fig. 6a and b, the lattice strain in the martensitic B19′ phase dramatically decreases at the edge of the transformation region and becomes compressive in the loading direction and tensile in the transverse direction. As one nears the austenitic region, the lattice strains in the martensitic B19′ phase become much more compressive (measured maximum: -1330 με) in the loading direction and tensile (measured maximum: 440 με) in the transverse direction. Like the martensitic B19′ phase, the austenitic B2 phase at the start of the transformation region exhibits low tensile strains in the loading direction and compressive strains in the transverse direction to loading. At the start of the transformation region, as one moves closer to the austenitic region, the lattice strain in the austenitic B2 phase becomes more tensile in the loading direction (maximum at 1090 με) and compressive in the transverse direction (maximum at -490 με) before gradually decreasing in the center of the austenitic region.

4. Discussion

4.1. Phase transformation zone

As illustrated in Figs. 5c and 6a and b, the average width of the entire transformation region is ~0.9 mm at the plateau stress (455 MPa) and at a constant macroscopic strain (5.7%). The phase transformation is clearly a localized process occurring over this region within the wire, whereas no transformation or deformation occurs in the rest of the gage length. The finite width of the transformation zone determined here is in good agreement with previous theoretical considerations that predict the zone to scale with the diameter of the specimen [70–72]. Moreover, our straightforward experimental analysis complements recent surface observations by digital image correlation [73] and modeling results on the strain fields in thin NiTi ribbon specimens which exhibit transformation zones with similar finite widths [30,74–76]. Furthermore, the austenitic B2 phase in the pseudoelastic NiTi wire almost completely transforms to martensite; only a small amount of residual austenite (less than 4 vol.%) is observed upon uniaxial loading above the stress plateau (at the end of the phase transformation), which has also been previously observed in coarse-grained NiTi [77] and predicted by micromechanical modeling [78].

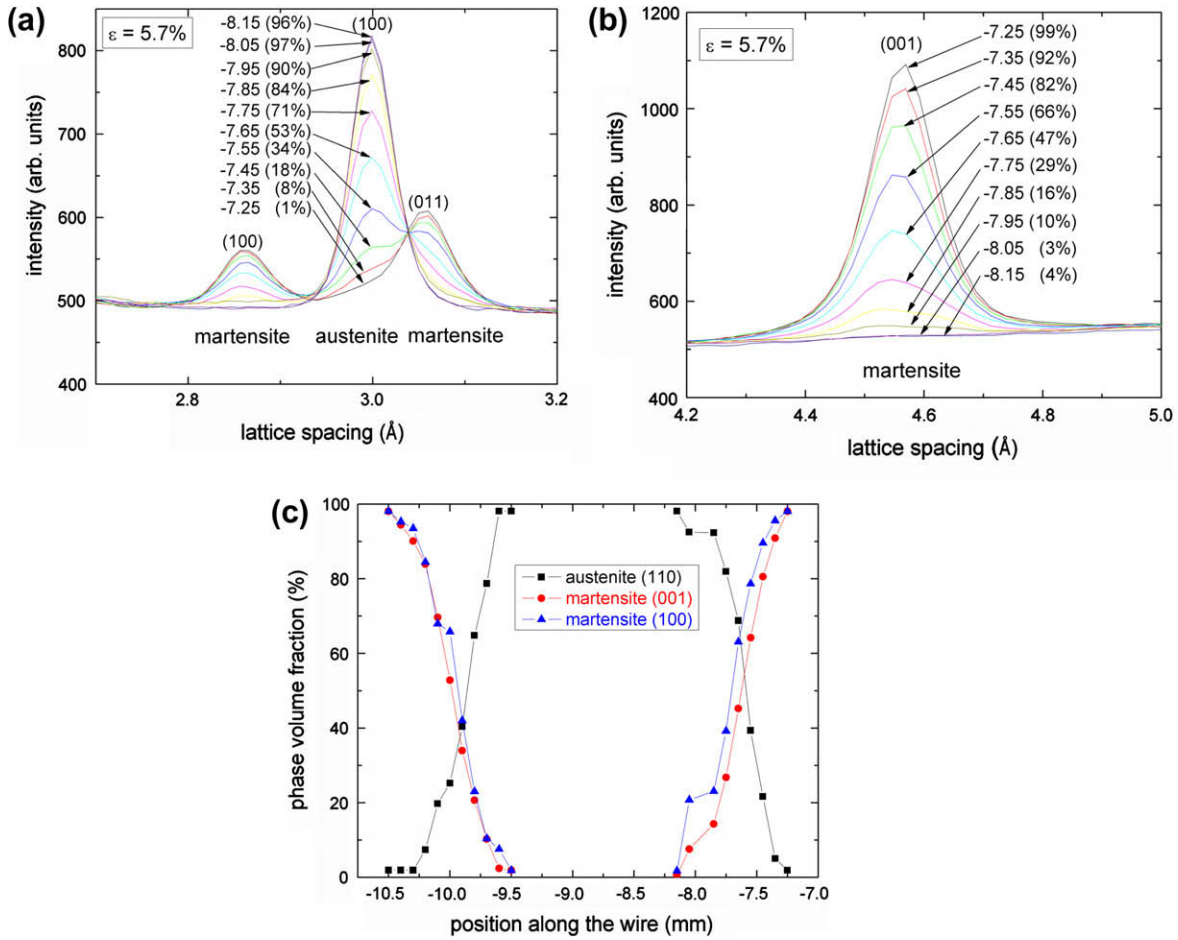

Fig. 5. Intensity vs. lattice spacing at a constant macroscopic strain (5.7%) for the (a) austenite B2 (1 0 0), martensite B19′ (1 0 0), and martensite B19′ (0 1 1), and (b) martensite (0 0 1) illustrating the phase volume fraction at each position along the NiTi SMA wire (x-axis). (c) The resulting phase volume fractions vs. position along the wire (x-axis) highlight the gradual phase transformation zones which are on average 0.9 mm in width.

By examining the lattice strains as illustrated in Fig. 6a and b, it can be shown that both the austenitic B2 and martensitic B19′ phases are highly strained in the transformation zone. In the loading direction (ε_{11} in Fig. 6a), the lattice plane for the austenitic B2 (1 0 0) reflection exhibits large tensile strains in the untransformed region. This tensile strain slightly increases (~100 με) when moving from the untransformed region to the phase transformation interface. Once the transformation begins, the tensile strains sharply decrease over the phase transformation zone before stabilizing to the level of the strain observed in the martensitic phase in the fully transformed, adjacent region. Conversely, at the onset of the phase transformation, the lattice plane for the martensitic B19′ (0 0 1) reflection experiences large compressive strains, which gradually decrease as more martensite transforms until equilibrium is reached at a low, but relatively constant, tensile strain of ~150 με.

Just before the austenite is fully transformed to martensite, the elastic lattice strain in the austenitic B2 phase becomes approximately equivalent to that of the martensitic B19′ phase. This result is particularly noteworthy since it suggests that, as more austenite is transformed to martensite, the strain in the austenite relaxes considerably. Therefore, the transformation requires lower stresses to occur as more austenite grains are surrounded by martensite grains. Moreover, the lattice strains in the martensitic B19′ phase remain relatively low and become tensile in the transformed region away from the phase transformation zone. This result suggests that, as the wire is loaded, the bulk of the load is being experienced at the phase transformation region and in the austenitic phase. This special strain state near the phase transformation region may be critical in stabilizing the localized mode of deformation. As the phase transition region propagates along the gage length, the maximum stresses act constantly in its direct vicinity and result in the formation of stress-induced martensite in the adjacent material.

4.2. Macro- and micro-strains in the austenitic B2 phase

As illustrated in Fig. 3, the macroscopic apparent modulus of austenite (56 GPa) during loading is approximately 20% higher than that observed upon unloading (45 GPa). In a pseudoelastic NiTi alloy which exhibited no R phase transformation during tensile testing, Liu and Xiang [62] also observed that the macroscopic apparent modulus for

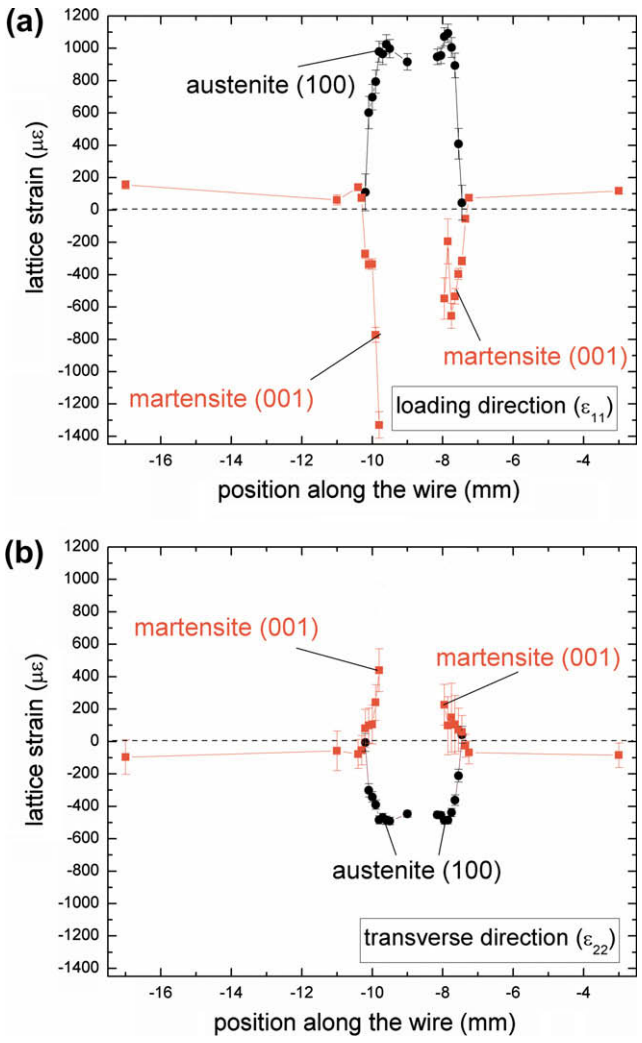

Fig. 6. Lattice strain (ε_{11} parallel and ε_{22} perpendicular to the applied stress) vs. the position along the NiTi wire for the austenitic B2 (1 0 0) and martensitic B19′ (0 0 1) reflections at a constant macroscopic strain (5.7%).

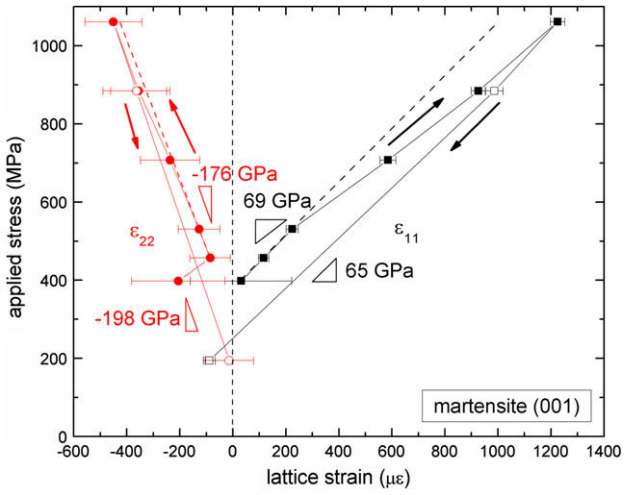

Fig. 7. Applied stress vs. lattice strain (ε_{11} parallel and ε_{22} perpendicular to the applied stress) at high loads for the martensite B19′ (0 0 1) reflection upon loading (closed data points) and unloading (open data points). The values of the slopes represent best fits of the first three (ε_{11}) and two (ε_{22}) data points from the loading data and for the last two points from the unloading data. The dashed lines indicate linear-elastic behavior.

austenite during loading is higher than that observed during unloading. This difference increased with increasing amount of strain. They attributed this softening of the slope to residual strains which are present after unloading and to an increase in the dislocation density after the forward and reverse transformation. Following their reasoning, the higher modulus value (56 GPa) in our macroscopic stress–strain data is most likely closer to the true Young's modulus of the austenitic material than is the unloading modulus value (45 GPa).

As expected and as shown by Rajagopalan et al. [27], individual austenite reflections exhibit different anisotropic behavior in compression than in tension. As noted by Vaidyanathan et al. [36], the anisotropy associated with different crystallographic directions in austenite during compressive loading results from a combination of elasticity, plasticity associated with slip, and phase transformation. Phase transformation does not account for the anisotropy associated with different crystallographic directions in our case, since martensite does not appear in the diffraction patterns until the stress plateau is reached. This implies that the anisotropy observed in our material, which is associated with different crystallographic directions, is only due to elasticity and plasticity associated with slip in the austenitic B2 reflections.

Lastly, a slight bend, which is generally accepted to be associated with the presence of R phase, observed in the macroscopic stress–strain curve at approximately 150 MPa, is also observed in the microscopic stress–strain curve at 177 MPa of the austenitic (2 1 1) reflection, while all other austenitic reflections remain essentially linear-elastic. This result suggests that the (2 1 1) reflection might be associated with the initiation of R phase or it might participate in load sharing between the R phase and austenitic phase. In general, however, the deformation mode of austenite remains mostly elastic.

4.3. Macro- and micro-strains in the stress-induced martensitic B19′ phase

The macroscopic modulus of martensite (25–28 GPa) during loading is more than 50% lower than that observed in the microscopic stress–strain curve (69 GPa, Fig. 7). Interestingly, and in contrast to the macroscopic observation, the microscopic modulus of martensite is also larger than that of austenite, which further confirms the results of recent ab initio investigations on the elastic properties of NiTi martensites [79]. Moreover, this result is in good agreement with observations made by Rajagopalan et al. [27], where they found that Young's modulus from the macroscopic stress–strain curve was 25–50% lower than that observed from the microscopic stress–strain curves created from lattice strains observed using neutron diffraction. They attribute this difference to the fact that the mac-

roscopic measurement includes, in addition to elastic strains (which are observed by neutron and synchrotron X-ray diffraction), ferroelastic twin orientation switching which was indicated by the observance of martensitic peak splitting during our in situ synchrotron X-ray diffraction test and results in additional strains, thus lowering the observed Young's modulus. Furthermore, in our case, difficulty in determining the elastic modulus of martensite from the macroscopic slope arises at least in part due to the fact that at the end of the phase transformation some strain is already present in the martensite. Besides this initial strain in the martensite, plastic deformation (austenitic) grain reorientation, and detwinning or reorientation of martensite variants all contribute to the macroscopic stress–strain curve [62,78].

The macroscopic modulus of martensite (18 GPa) during unloading is also more than 50% lower than that observed in the microscopic stress–strain curve (43 GPa). Similar to the results during loading, the much higher modulus observed using synchrotron X-ray diffraction is much closer to the true elastic modulus of this NiTi material. Moreover, it has been shown by Liu and Xiang [62] that the deviation of the apparent modulus of martensite between loading and unloading increases with increasing load due to a combination of deformation mechanisms. This behavior is not only observed in the macroscopic stress–strain curve, like that observed by Liu and Xiang [62], but it is also reflected in our microscopic stress–strain data.

4.4. Elastic lattice strains in the martensitic R phase

At 177 MPa in the microscopic stress–strain curve, the presence of the R phase is first observed during loading as a result of reaching a critical strain (~300 με) in the austenitic phase. Based on this observation, it is possible to confirm that the slight bend observed in the macroscopic stress–strain curve at approximately 150 MPa is due to the formation of R phase. It is likely that the R phase appears for the first time at a slightly lower load than at 177 MPa in the microscopic stress–strain curve, for example 150 MPa, where the slight bend is first observed in the macroscopic stress–strain curve.

As the applied stress increases, the amount of R phase increases as observed by an increase in the integrated peak intensity from synchrotron X-ray diffraction for the (1 1 0) and (2 2 0) R phase reflections. Furthermore, the lattice strains in the R phase continue to increase up to 1000 με before dropping to a constant strain value of approximately 200 με at the stress plateau. At the stress plateau, the dominating feature is the phase transformation zone where the strain becomes highly localized. Unlike the austenitic phase, the strain in the R phase remains essentially constant across the entire phase transformation interface before disappearing after the stress-induced martensitic transformation has occurred. This result suggests that R phase plays little role in the stress-induced phase transformation to martensite other than to soften the overall slope of the macroscopic stress–strain curve and to provide a small boost in the overall elastic strain (~1% or 1000 με) before the stress plateau is reached.

It is possible that strain in the austenite phase is transferred to the R phase. This does not appear to be the case here, although collecting more data points may further elucidate this behavior. As the macroscopic load increases, the stress in the austenite results in the formation of some R phase. Both phases seem to load elastically up until the stress plateau is reached. This is difficult to analyze in detail from our experimental data and requires smaller measuring increments (using two diffraction settings: normal exposure and overexposure to highlight strong and weak peaks, respectively) during loading to make this relationship clear. Normally, strain in one phase becoming constant is typically a result of load transfer from the softer phase to the stiffer reinforcement. This behavior in NiTi is interesting and could be due to some sort of load transfer before the martensite forms. It should be mentioned that the intermediate transformation from martensite to R phase before transforming back to austenite was not observed during unloading. It is likely that this intermediate transformation occurs below 400 MPa during unloading and before the reverse transformation zone. Further synchrotron experiments are currently underway to examine this region more thoroughly.

5. Summary and conclusions

The mechanical behavior of an ultrafine-grained pseudoelastic NiTi SMA wire was examined using synchrotron X-ray diffraction during in situ uniaxial tensile loading and subsequent unloading. From the results obtained in this study, several interesting conclusions, which shed new light on the nature of the mechanical behavior of NiTi SMAs, can be made:

(1) The phase transformation is a localized process. The transition zone between austenitic and martensitic regions is on average 0.9 mm wide (i.e. of a similar order of magnitude as the diameter of the thin wire). Although a small amount of residual austenite (less than 4 vol.%) was observed, the austenitic B2 phase is, for all practical purposes, fully transformed at loading above the stress plateau. At the austenite interface in the transformation zone, both the austenitic B2 and martensitic B19′ phases are highly strained (in tension and in compression, respectively, in the loading direction) just before phase transformation occurs. These strains gradually decrease until the phase transformation to martensite is complete. The martensitic B19′ phase exhibits a small constant tensile strain in all regions away from the phase transformation zone.
(2) Both the microscopic and macroscopic elastic moduli are within range of previously reported values for the austenitic and martensitic phases. The microscopic

modulus values confirm that the Young's modulus of martensite is higher than that of austenite. The Young's modulus from the macroscopic stress–strain curve is 25–50% lower than that observed from the microscopic stress–strain curves generated from lattice strains. This difference is due to the fact that the macroscopic measurement includes, in addition to elastic strains (which are observed by neutron and synchrotron X-ray diffraction), ferroelastic twin orientation switching which was suggested by the observance of martensitic peak splitting during our in situ synchrotron X-ray diffraction test and results in additional strains thus lowering the apparent Young's modulus. Furthermore, an initial amount of strain is present at the end of the stress plateau. Besides initial strain in the martensite, plastic deformation, grain reorientation, and detwinning and reorientation of martensite variants may also contribute to the macroscopic stress–strain curve.

(3) A slight bend is observed in the macroscopic stress–strain curve due to the emergence of R phase. The lattice strains of the austenitic B2 phase are predominantly linear-elastic with the exception of the (2 1 1) reflection, which suggests that some austenitic reflections are associated with the R phase transformation or participate in load sharing between the R phase and austenitic phase. The presence of R phase lowers the overall slope of the macroscopic stress–strain curve and provides a small increase in the overall elastic strain ($\sim$1% or 1000 $\mu\varepsilon$) at stresses below the stress plateau.

Acknowledgements

The authors acknowledge funding from the Deutsche Forschungsgemeinschaft (DFG) and the Wissenschaftsministerium Nordrhein-Westfalen (NRW) in the framework of the research center SFB 459 ("Shape Memory Technology") at the Ruhr-University Bochum and by the Helmholtz Virtual Institute VH-VI-102. The authors further acknowledge funding from the DFG through the research group FOR 544 on Ultra Fine Grained (UFG) metallic materials coordinated by H.J. Maier (University of Paderborn). M.L. Young acknowledges funding by the Alexander von Humboldt Foundation. M.F.X.W. acknowledges funding through the Emmy Noether program of the DFG and by the North Rhine Westfalian Academy of Science.

References

[1] Otsuka K, Ren X. Intermetallics 1999;7:511.
[2] Otsuka K, Wayman CM. Shape memory materials. Cambridge and New York: Cambridge University Press; 1998.
[3] Morgan NB. European symposium on martensitic transformation and shape-memory. Mater Sci Eng A 2004;378:16.
[4] Van Humbeeck J. Mater Sci Eng A 1999;273–275:134.
[5] Duerig T, Pelton A, Stockel D. Mater Sci Eng A 1999;273–275:149.
[6] Hornbogen E. In: Bunk WGJ, editor. Advanced structural and functional materials. Heidelberg: Springer-Verlag; 1991. p. 133.
[7] Saburi T. Shape memory materials. In: Otsuka K, Wayman CM, editors. Cambridge: Cambridge University Press; 1998. p. 49.
[8] Mentz J, Frenzel J, Wagner MF-X, Neuking K, Eggeler G, Buchkremer HP, et al. Mater Sci Eng A 2008;491:270.
[9] Eggeler G, Hornbogen E, Yawny A, Heckmann A, Wagner M. European symposium on martensitic transformation and shape-memory. Mater Sci Eng A 2004;378:24.
[10] Wagner MF-X, Eggeler G. Mech Mater 2006;38:1012.
[11] Wagner MF-X, Nayan N, Ramamurty U. J Phys D 2008;41:185408-1.
[12] McKelvey AL, Ritchie RO. J Biomed Mater Res, Part A 1999;47:301.
[13] Vaidyanathan R, Dunand DC, Ramamurty U. Mater Sci Eng A 2000;289:208.
[14] Sawaguchi T, Kausträter G, Yawny A, Wagner M, Eggeler G. Metall Mater Trans A 2003;34:2847.
[15] Wagner M, Sawaguchi T, Kausträter G, Höffken D, Eggeler G. Mater Sci and Eng A. In: European symposium on martensitic transformation and shape-memory 2004;378:105.
[16] Wagner MF-X, Eggeler G. Int J Mater Res 2006;97:1687.
[17] Olbricht J, Wagner MF-X, Condó A, Dlouhy A, Grossmann C, Kroeger A, et al. Int J Mater Res 2008;99:1150.
[18] Khalil Allafi J, Schmahl WW, Toebbens DM. Acta Mater 2006;54:3171.
[19] Hara T, Ohba T, Okunishi E, Otsuka K. Mater Trans JIM 1997;38:11.
[20] Khalil Allafi J, Ren X, Eggeler G. Acta Mater 2002;50:793.
[21] Yawny A, Sade M, Eggeler G. Z Metallk 2005;96:608.
[22] Kulkov SN, Mironov YP. Nucl Instrum Methods Phys Res A 1995;359:165.
[23] Schuster A, Voggenreiter HF, Dunand DC, Eggeler G. J Phys IV 2003;112:1177.
[24] Daymond MR, Young ML, Almer JD, Dunand DC. Acta Mater 2007;55:3929.
[25] Gollerthan S. Untersuchungen zum Bruchverhalten von NiTi-Formgedaechtnislegierungen. PhD thesis (in German). Ruhr Universität Bochum, 2007.
[26] Gollerthan S, Herberg D, Baruj A, Eggeler G. Mater Sci Eng A 2007;481–482:156.
[27] Rajagopalan S, Little AL, Bourke MAM, Vaidyanathan R. Appl Phys Lett 2005;86:081901.
[28] Khalil-Allafi J, Schmahl WW, Wagner M, Sitepu H, Toebbens DM, Eggeler G. Mater Sci Eng A 2004;378:161.
[29] Khalil Allafi J, Hasse B, Kloenne M, Wagner M, Pirling T, Predki W, Schmahl WW. Materialwiss Werkstofftech 2004;35:280.
[30] Schmahl WW, Khalil-Allafi J, Hasse B, Wagner M, Heckmann A, Somsen C. European symposium on martensitic transformation and shape-memory. Mater Sci Eng A 2004;378:81.
[31] Robertson SW, Mehta A, Pelton AR, Ritchie RO. Acta Mater 2007;55:6198.
[32] Hasan M, Schmahl WW, Hackl K, Heinen R, Frenzel J, Gollerthan S, et al. Mater Sci Eng A 2008;481–482:414.
[33] Mehta A, Gong X-Y, Imbeni V, Pelton A, Ritchie RO. Adv Mater 2007:19.
[34] Bourke MAM, Vaidyanathan R, Dunand DC. Appl Phys Lett 1996;69:2477.
[35] Khalil Allafi J, Eggeler G, Schmahl WW, Sheptyakov D. Mater Sci Eng A 2006;438:593.
[36] Vaidyanathan R, Bourke MAM, Dunand DC. J Appl Phys 1999;86:3020.
[37] Vaidyanathan R, Bourke MAM, Dunand DC. Mater Sci Eng A 1999;273–275:404.
[38] Raghunathan SL, Azeem MA, Collins D, Dye D. Scripta Mater 2008;59:1059.
[39] Sittner P, Novak V, Landa M, Lukas P. Mater Sci Eng A 2007;462:12.

[40] Sittner P, Landa M, Lukas P, Novak V. Mech Mater 2006;38:475.
[41] Sittner P, Lukas P, Novak V, Daymond MR, Swallowe GM. Mater Sci Eng A 2004;378:97.
[42] Shaw JA, Kyriakides J. J Mech Phys Solids 1995;43:1243.
[43] Shaw JA, Kyriakides J. Acta Mater 1997;45:683.
[44] Shaw JA, Kyriakides J. Int J Plast 1997;13:837.
[45] Miyazaki S, Imai T, Otsuka K, Suzuki Y. Scripta Metall 1981;15:853.
[46] Favier D, Louche H, Schlosser P, Orgeas L, Vacher P, Debove L. Acta Mater 2007;55:5310.
[47] Sun QP, Li ZQ. J Solids Struct 2002;39:3797.
[48] Leo PH, Shield TW, Bruno OP. Acta Metall Mater 1993;41:2477.
[49] Olbricht J, Schaefer A, Wagner MF-X, Eggeler G. Characterization of transformation localization during pseudoelastic cycling of NiTi. In: Miyazaki S, editor. SMST 2007. Japan: ASM International; 2007. p. 47.
[50] Khalil Allafi J, Schmahl WW, Reinecke T. Smart Mater Struct 2005;14:192.
[51] Gollerthan S, Young ML, Baruj A, Frenzel J, Schmahl WW, Eggeler G. Acta Mater 2009;57:1015.
[52] Dwight AE. CsCl-Type Trans Metal Soc AIME 1959;215:283.
[53] Goryczka T, Morawiec H. J Alloys Compd 2004;367:137.
[54] Kudoh Y, Tokonami M, Miyazaki S, Otsuka K. Acta Metall 1985;33:2049.
[55] Hammersley AP. ESRF97HA02T, FIT 2D: an introduction and overview. ESRF internal report; 1997.
[56] Hammersley AP. ESRF98HA01T, FIT 2D V9.129 reference manual V3.1. ESRF internal report; 1998.
[57] MATLAB M. <http://www.mathworks.com>.
[58] Young ML, Almer JD, Lienert U, Daymond MR, Haeffner DR, Dunand DC. Acta Mater 2007;55:1999.
[59] Wanner A, Dunand DC. Metall Mater Trans A 2000;31:2949.
[60] Almer JD, Lienert U, Peng RL, Schlauer C, Oden M. J Appl Phys 2003;94:697.
[61] Young ML, DeFouw JD, Almer JD, Haeffner DR, Dunand DC. Acta Mater 2007;55:3467.
[62] Liu Y, Xiang H. J Alloys Compd 1998;270:1.
[63] Gall K, Tyber J, Brice V, Frick CP, Maier HJ, Morgan N. J Biomed Mater Res, Part A 2005;75:810.
[64] Frick CP, Ortega AM, Tyber J, Gall K, Maier HJ. Metall Mater Trans A 2004;35:2013.
[65] Zadno GR, Duerig TW. Linear and non-linear superelasticity in NiTi. In: Otsuka K, Shimizu K, editors. MRS international meeting on advanced materials, vol. 9. Pittsburgh (PA): Materials Research Society; 1989. p. 201.
[66] Sakuma T, Mihara Y, Toyama H, Ochi Y, Yamauchi K. Mater Trans, JIM 2006;47:787.
[67] Pfetzing J, Schaefer A, Somsen C, Wagner MF-X. Int J Mater Res 2009;100:936.
[68] Norfleet DM, Sarosi PM, Manchiraju S, Wagner MF-X, Uchic MD, Anderson PM, et al. Acta Mater 2009;57:3549.
[69] Reed-Hill RE, Abbaschian R. Physical metallurgy principles. Boston (MA): PWS Publishing Company; 1994.
[70] Messner C, Reisner G, Sun QP, Werner E. Comput Mater Sci 2000;19:313.
[71] Sun QP, Zhong Z. Int J Plast 2000;16:1169.
[72] Soul H, Yawny A, Lovey FC, Torra V. Mater Res 2007;10:387.
[73] Schaefer A, Wagner MF-X. Strain mapping at propagating interfaces in pseudoelastic NiTi. In ESOMAT 2009 – The 8th European Symposium on Martensitic Transformations, 06031, Sittner P, Heller L, Paidar V, editors. In: EDP Sciences (www.esomat.org); 2009. doi:10.1051/esomat/200906031.
[74] Grossmann C, Schaefer A, Wagner MF-X. Mater Sci Eng A 2010;527:1172.
[75] Grossmann C, Schaefer A, Wagner MF-X. Finite element simulation of localized phase transformations in pseudoelastic NiTi shape memory alloys subjected to multi-axial stress-states. In: ICOMAT 2008, Santa Fe, NM, in press.
[76] Schmahl WW, Baruj A, Khalil Allafi J, Nebel H, Hasan M. High-energy synchrotron diffraction study of transformation shear bands in Ni-rich NiTi shape memory alloys. In: Mertmann M, editor. Shape memory and superelastic technologies. Baden–Baden, SMST-2004. Materials Park (OH): ASM International; 2004. p. 69.
[77] Brinson LC, Schmidt I, Lammering R. J Mech Phys Solids 2004;52:1549.
[78] Heinen R, Hackl K, Windl W, Wagner MF-X. Acta Mater 2009;57:3856.
[79] Wagner MF-X, Windl W. Acta Mater 2008;56:6232.